Chinese Chemical Letters 32 (2021) 2787–2791

Contents lists available at ScienceDirect

Chinese Chemical Letters

journal homepage: www.elsevier.com/locate/cclet

Communication

A carbon-rich g-C_3N_4 with promoted charge separation for highly efficient photocatalytic degradation of amoxicillin

Dan Huang[a], Xianbo Sun[a], Yongdi Liu[a], Haodong Ji[b], Wen Liu[b], Chong-Chen Wang[c], Weiyu Ma[a], Zhengqing Cai[a,*]

[a] National Engineering Laboratory for High-concentration Refractory Organic Wastewater Treatment Technologies, East China University of Science and Technology, Shanghai 200237, China
[b] The Key Laboratory of Water and Sediment Sciences, Ministry of Education, College of Environmental Sciences and Engineering, Peking University, Beijing 100871, China
[c] Beijing Key Laboratory of Functional Materials for Building Structure and Environment Remediation, School of Environment and Energy Engineering, Beijing University of Civil Engineering and Architecture, Beijing 100044, China

ARTICLE INFO

Article history:
Received 4 November 2020
Received in revised form 12 December 2020
Accepted 7 January 2021
Available online 12 January 2021

Keywords:
Carbon-rich g-C_3N_4
Photocatalysis
Built-in electron field
Charge separation

ABSTRACT

A novel carbon-rich g-C_3N_4 nanosheets with large surface area was prepared by facile thermal polymerization method using urea and 1,3,5-cyclohexanetriol. Plenty of carbon-rich functional groups were introduced into the surface layers of g-C_3N_4, which constructed the built-in electric field (BIEF) and resulted in improved charge separation; therefore, the carbon-rich g-C_3N_4 displayed superior photocatalytic activity for amoxicillin degradation under solar light. The contaminant degradation mechanism was proposed based on radical quenching experiments, intermediates analysis and density functional theory (DFT) calculation. Moreover, the reusing experiments showed the high stability of the material, and the amoxicillin degradation under various water matrix parameters indicated its high applicability on pollutants treatment, all of which demonstrated its high engineering application potentials.

The overuse of antibiotics in medical treatment and animal farming have caused the discharge of huge amount of antibiotics into natural water environment, leading the propagation of antibiotic resistance genes (ARGs), and created risks to aquatic lives and public health [1]. Amoxicillin (AMX) is a widely used antibiotic, and commonly detected in surface water due to its poor metabolism by microorganisms [2]. Various technologies have been developed to remove antibiotics from water, such as biological technology and advanced oxidation processes (AOPs). Among various AOPs, the photocatalysis, especially with solar light active catalysts, has attracted great attention due to its low-cost, high efficiency and environmental friendliness.

Graphitic carbon nitride (g-C_3N_4) is one of the most intensively studied photocatalyst due to its facile synthesis, high stability and easy functionalization. However, the bulk g-C_3N_4 shows limited photocatalytic activity owing to fast electron-hole recombination rate, relative low surface area and limited active sites [3]. Many efforts have been devoted to overcome these drawbacks, such as constructing heterojunctions, doping with metal/non-metal, adjusting the morphology, *etc*. Among them, tailoring g-C_3N_4 by surface modification has been considered as a new approach to modify the photocatalysts [4]. Benefit from weak van der Waals force between layers [5], doping with heteroatoms (S, N, O, *etc*.) or introducing function groups in g-C_3N_4 can be applied to modify the electronic structure and bandgap *via* inducing electron redistribution and lattice distortion or acting as charge trapping center [6]. Constructing built-in electric field (BIEF) is another modification method, which could efficiently drive light-induced electrons and holes to migrate reversely, leading to higher separation efficiency [7].

Herein, we reported the preparation of a porous carbon-rich g-C_3N_4 *via* pyrolysis of a mixture of urea and 1,3,5-cyclohexanetriol (90 mg of 1,3,5-cyclohexanetriol was added for the optimal composite and which is denoted as C-CN90). The surface of the obtained C-CN90 was modified by a functional group of graphited conjugated construction (π), which offered the material with: (1) Abundant adsorption sites with plentiful functional groups, (2) lowered electron-hole recombination rate induced by constructed

* Corresponding author.
E-mail address: caizhengqing@ecust.edu.cn (Z. Cai).

https://doi.org/10.1016/j.cclet.2021.01.012

BIEF. Therefore, the C-CN90 showed superior activity on the photocatalytic degradation of AMX. In this work, various characterization methods were applied to elucidate the promoted photocatalytic activity of the material, and radical quenching experiments, HPLC-MS analysis and density functional theory (DFT) calculation were conducted to reveal the photocatalytic degradation mechanism of AMX. Moreover, response surface methodology (RSM) and material reusing experiments were applied to assess its environmental application potential.

The X-ray diffraction (XRD) of samples revealed the diffraction peaks at 13.1° and 27.8° (Fig. S1 in Supporting information), corresponding to the (100) and (002) planes of g-C_3N_4 (JCPDS No. 87-1526) [8]. The dramatically decreased peak intensity indicated weaker crystallinity due to the introduction of carbon-rich functional groups. Meanwhile, the diffraction peaks of g-C_3N_4 had no obvious change after five reusing cycles, suggesting that C-CN90 had favorable stability, which was also confirmed by material reusing tests.

TEM images revealed that g-C_3N_4 had dense and thick two-dimension (2D) nanoflakes structure (Fig. 1a), while the C-CN90 was less agglomeration ultra-thin (2D) nanoflakes structure (Fig. 1b), which indicated that the heat etching in the presence of 1,3,5-cyclohexanetriol is favorable for the formation of thinner layered g-C_3N_4. This result is consistent with the larger specific surface area of C-CN90 that revealed by BET analysis (Table S1 in Supporting information). Fig. 1c was TEM image and the corresponding EDS elemental mapping images were shown as Fig. 1d and e. The larger surface area of C-CN90 could provide more active sites and expedite the mass transfer for photocatalytic reactions. The elemental mappings showed that C and N are homogeneously distributed in the C-CN90, but it is worth noting that distinctly stronger C signal (in yellow) was observed on the C-CN90 nanosheets, and the EDS results revealed that the C ratio of C-CN90 is significantly higher than g-C_3N_4. This result is in accord with the obtained C/N atomic ratio by XPS, which is 1.01 for C-CN90 and 0.84 for g-C_3N_4 (Table S2 in Supporting information). Therefore, the higher C/N revealed the formation of carbon-rich functional groups in C-CN90, the interaction between carbon-rich functional groups and g-C_3N_4 would be favorable for the interfacial charge transfer and migration, thus vastly suppressing the recombination of photo-generated electron-hole pairs.

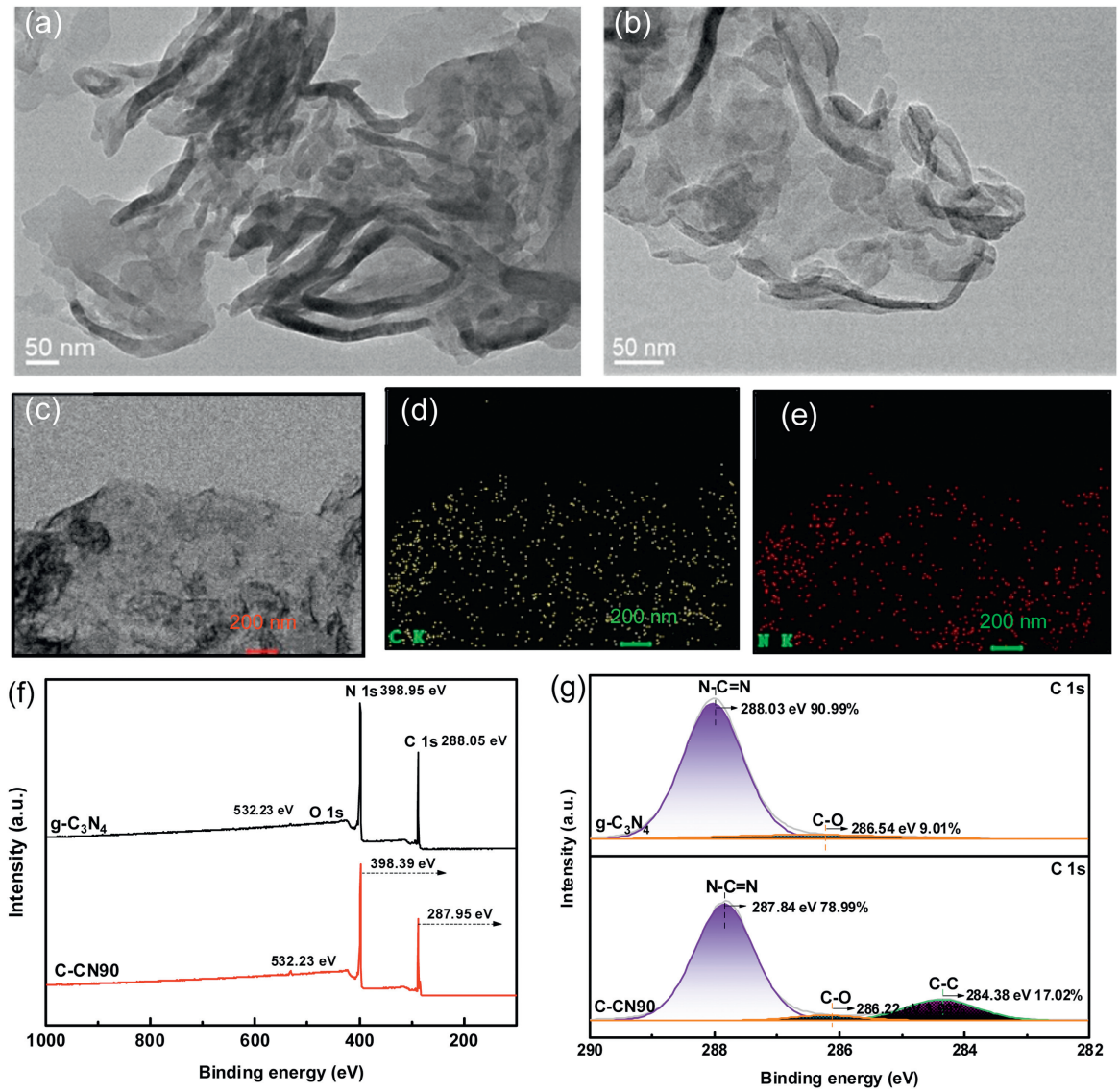

Fig. 1. TEM images of (a) g-C_3N_4 and (b) C-CN90; (c) TEM image and (d, e) C and N elements distribution mapping of C-CN90. (f) The survey spectra, and (g) XPS spectra of C 1s of g-C_3N_4 and C-CN90.

Moreover, the adsorption/desorption isotherm (BET) of two samples can be classified into type IV with H3 hysteresis loop (Fig. S2 in Supporting information), indicating the presence of mesopore structures and layered structure [9] as confirmed by TEM. The larger surface area and abundant carbon-rich functional group offered more active sites for the photocatalytic degradation of AMX.

XPS was performed as shown in Figs. 1f and g, the peaks in the survey spectra were assigned to C 1s, N 1s, O 1s, where the trace O element (about 2 at%) may result from the calcination of urea [10]. The g-C_3N_4 peaks located at 288.03 and 286.54 eV were ascribed to N—C=N bonds in N-containing aromatic ring and C—O bonds, respectively (Fig. 1g) [11]. While the new peak appeared at 284.38 eV for C-CN90 was assigned to the C—C bonds of the graphitic carbon (π-excitation) [12], indicating the formation of graphited conjugated construction. The N 1s spectra (Fig. S3 in Supporting information) of two samples displayed no distinction. It should be noted that the peaks ascribed to the N—C=N of g-C_3N_4 shifted to lower binding energy for both C 1s and N 1s spectra (Fig. S4 in Supporting information), implying the interaction of graphited conjugated construction coupled with g-C_3N_4, which is in favor of improving the charge carriers transfer and separation efficiency thus enhance photocatalytic performance [13].

The UV–vis DRS analysis (Fig. 2a, Fig. S5 in Supporting information) showed that the absorption edges of g-C_3N_4, C-CN60, C-CN90 and C-CN120 (the C-CNx synthesized with addition of 60, 90 and 120 mg of 1,3,5-cyclohexanetriol) were ~423, 449, 474 and 462 nm, respectively. Obviously, the carbon-rich functional groups narrowed the optical bandgap (E_g) of C-CN90, enabled the utilization of solar irradiation to longer wavelength, which explained why C-CN90 shown superior photocatalytic performance than C-CN120 and C-CN60. Generally, the flat-band potentials (E_{fb}) of the samples were measured using Mott-Schottky plots [14]. Fig. S6 (Supporting information) showed M–S plots of g-C_3N_4 and C—CN, and the positive slope indicated that they are n-type semiconductors [15]. The E_{fb} of g-C_3N_4 and C-CN90, based on the x intercept of the linear region, were determined to be −0.45 and −0.50 eV (*vs.* NHE), respectively. In general, the flat band potential of a semiconductor is equal to its Fermi level [16]. For n-type semiconductor, the bottom of the conduction band (CB) is more negative (about 0.2 eV) than Fermi level [17]. Therefore, the energy of conduction band (E_{CB}) of g-C_3N_4 and C—CN were determined as −0.65 eV and −0.70 eV, respectively. Based on the E_g obtained by UV–vis DRS, the energy of valence band (E_{VB}) of g-C_3N_4 and C-CN90 were calculated as 2.35 eV and 1.91 eV, respectively. The result is close to the XPS valence band spectra (as shown in Fig. 2b).

The separation efficiency of photogenerated electron-hole pairs is crucially important for the activity of photocatalyst, and which was revealed by electrochemical impedance spectra (EIS) and photocurrent-time curves in Fig. 2c and Fig. S7 (Supporting information). The EIS Nyquist plots of C-CN90 showed the smallest arc radius, indicating its highest charge separation efficiency; consistently, the C-CN90 also showed the highest current density, further confirming its fastest charge separation rate during the photocatalysis process [18]. Moreover, all the C-CNx samples showed decreased resistance value and promoted photocurrent density, suggesting the introduction of C elements in g-C_3N_4 is an effective approach to accelerate the interfacial charge-carrier separation. Therefore, the results revealed in Fig. S8 (Supporting information) indicated that the carbon-rich functional groups in g-C_3N_4 narrowed the band gap and facilitated the charge separation, both of which are beneficial for improving the photocatalytic activity of the materials. Therefore, the new materials are supposed to exhibit higher photocatalytic activity on contaminants degradation.

Based on the material characterizations, the scheme of BIEF was proposed in Scheme 1, which demonstrated the effectiveness of surface carbon-rich groups doping on the energy bands. Theoretically, the surface layer of g-C_3N_4 was more likely doping by carbon-rich functional groups, while the inner layer tends to preserve the original band structure [19]. It was noted that the fermi levels of g-C_3N_4 and C-CN90 were derived as −0.50 eV and −0.45 eV from the Mott-Schottky plots (Fig. S6), respectively. Therefore, the doped carbon-rich functional groups could lead to a more negative fermi level, and the electron will move from surface layers to inner layers until achieving Fermi equilibrium [20], resulting in the positive charged surface layers and negative charged inner layers. Hence, the construction of internal BIEF was constructed (Scheme 1). Under solar light irradiation, the BIEF could drive the electrons to migrate from the inner to the surface layer, however, the light-induced holes still stayed in original layers because of the high barrier resulted from the BIEF. Therefore, the separation efficiency of light-induced electrons/holes was significantly improved by construction of BIEF, which was confirmed by EIS plots and PL spectra (Figs. 2c and d). Moreover, electrons accumulated on the surface layer could react with O_2 to generate superoxide radicals ($O_2^{\bullet-}$) ($O_2 + e^- \rightarrow {}^{\bullet}O_2$), resulting in the promoted AMX degradation.

The photocatalytic performance of the prepared materials was evaluated by the degradation of AMX in aqueous phase under simulated solar or visible light irradiations (experimental details were included in Text S4, adsorption kinetic was shown in Fig. S9 in Supporting information). As shown in Figs. 3a and b, no significant decrease in AMX concentration was observed in the absence of photocatalysts, while all C-CNx samples showed higher activity than g-C_3N_4, and follows the order of: C-CN90 > C-CN60 > C-CN120 > g-C_3N_4 under both solar and visible light. As demonstrated in the inset figure of Figs. 3a and b, all the degradation kinetics follow the first-order law, the rate constants are 0.012 and 0.0047 min^{-1}, respectively, for C-CN90 under solar and visible light, which is 2.3 and 3.9 times of g-C_3N_4 (Fig. 3c). The results indicated that the incorporation of carbon-rich construction in g-C_3N_4 significantly improved the visible light activity, which is well matched with UV–vis DRS characterization in Fig. 2a. However, when compared materials with different rich-carbon functional groups loading, the visible light activity were less varied, but the

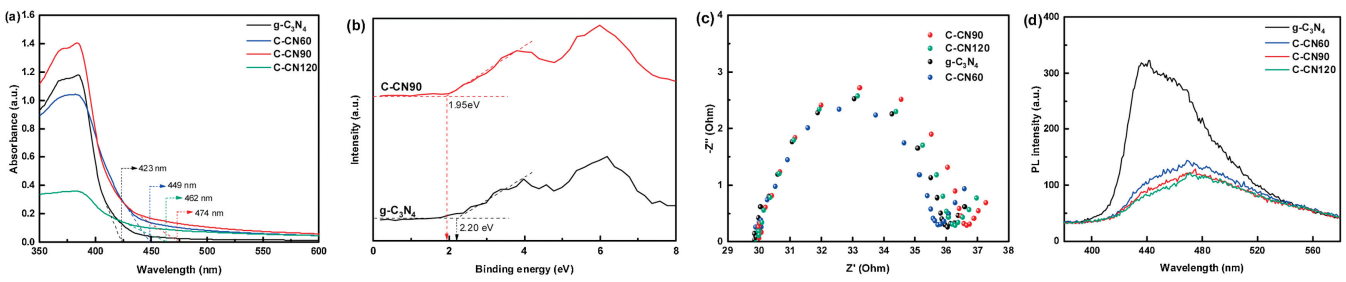

Fig. 2. (a) UV–vis DRS spectra. (b) XPS valence band spectra of g-C_3N_4 and C-CN90. (c) EIS Nyquist plots. (d) Photoluminescence (PL) spectra of g-C_3N_4 and C-CNx.

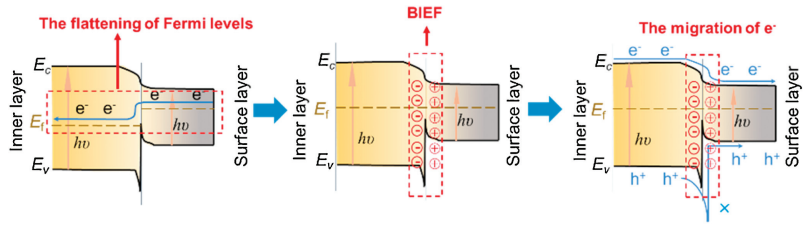

Scheme 1. The scheme of BIEF by flattening of fermi levels.

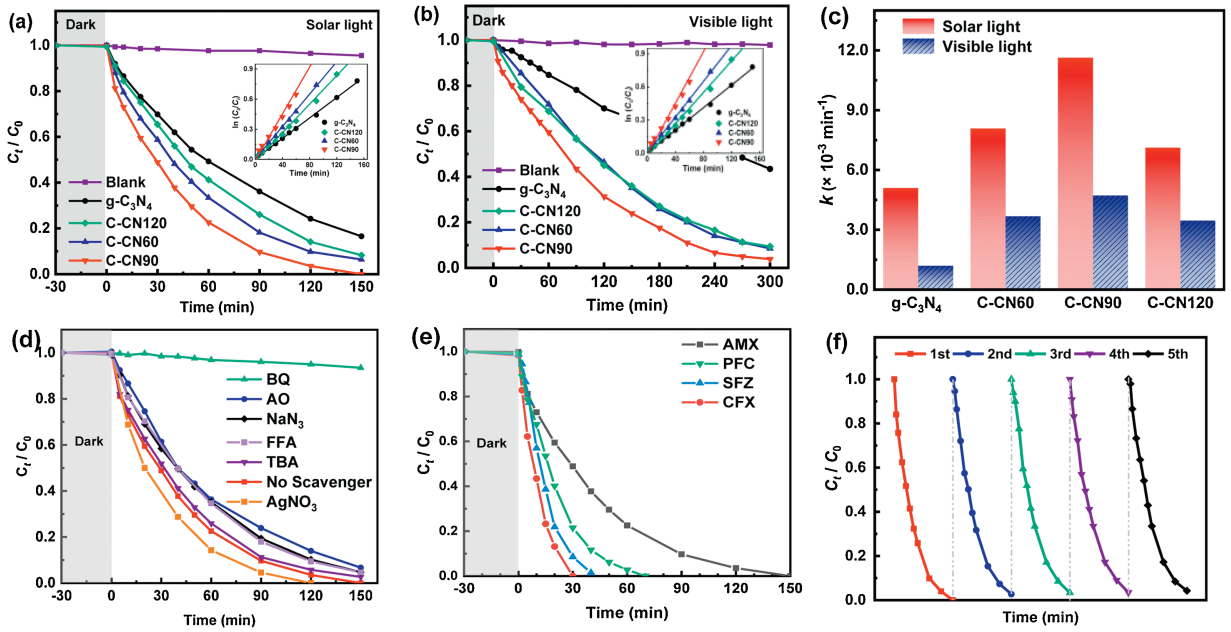

Fig. 3. Photocatalytic degradation kinetics of AMX by the synthesized materials under (a) simulate solar light, and (b) visible light. (c) AMX degradation rate constants under solar and visible light. (d) The effects of various scavengers on the photocatalytic degradation of AMX, and (e) the photocatalytic degradation of various antibiotics over C-CN90. (f) Reusing experiments of C-CN90 for the degradation of AMX in 5 cycles.

solar light activity for the optimal material was much higher than other materials, indicating the presence of carbon-rich groups provided the materials with improved visible light activity [21], and the dosage of carbon-rich groups had high impact on the promoted charge separation efficiency as revealed in Fig. 3c.

To further reveal the photocatalytic degradation mechanism by C-CN90, the contributions of reactive species on AMX degradation were evaluated with the presence of different radical scavengers (Fig. 3d). The photocatalytic degradation of AMX was significantly inhibited by benzoquinone (BQ, a $O_2^{\bullet-}$ scavenger), revealing the critical role of $O_2^{\bullet-}$ in the photocatalysis system; while the insignificant decrease in AMX degradation with *tert*-butanol (TBA, a $^{\bullet}OH$ scavenger) indicated that $^{\bullet}OH$ played a negligible role; and the weak decreased AMX removal rates in the presence of NaN_3 (a $^1O_2$ and $^{\bullet}OH$ scavenger) and furfuryl alcohol (FFA, a $^1O_2$ quencher) implied that $^{\bullet}OH$ was not involved in the reaction and $^1O_2$ played a negligible role. The slight decrease in the presence of ammonium oxalate (AO, an h^+ quencher) indicated that h^+ had little effect on AMX removal. Notably, adding $AgNO_3$ (an e^- quencher) significantly improved the removal of AMX, which can be due to the trapping of electron by $AgNO_3$, and thus promoted the charge separation [22]. Therefore, the contribution of radicals in the photocatalytic system follows the order: $O_2^{\bullet-} > e^- > h^+ > {}^1O_2$. The standard redox potential of $O_2/O_2^{\bullet-}$ (−0.33 eV) is lower than the CB of C-CN90 [8], thus the accumulated electrons on the surface of C-CN90 generated large amount of $O_2^{\bullet-}$. However, the standard redox potential of $^{\bullet}OH/OH^-$ (2.3 eV) is higher than the VB of C-CN90 (1.85 eV) [23], therefore, $^{\bullet}OH$ is not likely to appear in this photocatalysis system.

The degradation intermediates of AMX were identified using LC–MS, combined with the Fukui index based on the density functional theory (DFT) calculation, the possible degradation pathway of AMX was proposed in Fig. S10 (Supporting information). Fukui index electrophilic attack (f^-) and radical attack (f^0) of atoms on AMX molecule were shown in Table S3 and Fig. S11 (Supporting information), respectively. Specifically, the S44 marked in yellow displayed highest f^- and f^0, suggesting S44 is vulnerable to both electrophilic attack (f^-) and radical attack (f^0). It is known that $O_2^{\bullet-}$ react with AMX *via* radical attack [24], and two AMX decomposition pathways were proposed. The pathway 1 begun based on the fact that the two atoms of double bond (C=O, C24 and O28) displayed higher f^-, suggesting the double bond (C=O) was easy to be attacked by electrophilic attack. In the reaction, the hydrolysis of AMX firstly led to the formation of AMX penicilloic acids (P1, *m/z* 383), which was assigned based on their characteristic fragmentation peaks at *m/z* 349 and *m/z* 160. The double bond (C=O) attached on the *β*-lactam ring was then attacked by $O_2^{\bullet-}$, leading to the generation of P2 (*m/z* 340). In the pathway 2, deamination reaction occurred due to the loss of $-NH_2$ and the intermediates P3 (*m/z* 349) was produced. The further

oxidation formed intermediates with smaller carboxyl groups, *i.e.,* the intermediate with *m/z* of 116, and gradually mineralized into CO_2 and H_2O after sufficient reaction time.

The engineering application potential of synthesized material was evaluated by conducting photocatalysis experiments with various antibiotics, under various water parameters, and material reusing experiments. As typical antibiotic species of quinolones, sulfonamides and cephalosporins, the pefloxacin (PFC), sulfathiazole (SFZ) and cefalexin (CFX) showed comparable photocatalytic degradation efficiency with AMX under identical conditions (Fig. 3e), revealing that C-CN90 also owns superior performance on removing other pharmaceutical pollutants. The C-CN90 can be easily recycled by simple filtration, and its photocatalytic activities on AMX degradation only slight decreased after five reusing cycles (Fig. 3f). The XRD patterns (in Fig. S1) revealed that the peak intensity of the used C-CN90 did not significantly change, confirming its good stability. The Box-Behnken experimental design methodology was used to reveal the effects of water parameters on the photocatalysis performance (Tables S4 and S5 in Supporting information). The quadratic model ($Y = 0.0064 - 0.0038A - 0.0044B + 0.016A^2$, where Y is the AMX degradation rate constants) was obtained based on the experimental results. Small *P* values ($P < 0.05$) and high *F* values from ANOVA (Table S6 in Supporting information) assured that the model is significant [25]. According to the *F* values, the contributing factors of various water parameters on photocatalysis follows the order of: $HA > pH > SO_4^{2-}$. Notably, there was not significant interaction between any two factors (AB, AC, BC for $P > 0.05$), and the 3D response surface and its corresponding 2D contour plots were produced in Fig. S12 (Supporting information). Therefore, the AMX removal was more remarkably affected by pH, especially the neutral pH (5∼7) significantly decreased the AMX removal, which can be due to the improved electrostatic attraction between the negatively charged AMX [26] and the positively charged AMX at $pH < 5.4$ [21,27], and the faster hydrolysis of AMX under alkaline conditions (pH 7∼10) [28]. The SO_4^{2-} or DOM did not significant affect the photocatalysis performance of C-CN90. Therefore, the C-CN90 owned excellent stability and applicability, and had great engineering application potential.

In summary, a highly active g-C_3N_4 was synthesized by introducing graphited conjugated construction into the surface of g-C_3N_4, the interaction between g-C_3N_4 and graphited conjugated construction narrowed the band gap and improve the separation of photogenerated electron-hole pairs, resulting in the enhanced photocatalytic performance of AMX degradation. The photocatalytic degradation mechanism and its engineering application potential were thoroughly investigated. This study provided an effective approach to synthesize highly active photocatalyst coupling with carbon-rich functional groups for water remediation.

Declaration of competing interest

The authors declare that they have no known competing financial interests or personal relationships that could have appeared to influence the work reported in this paper.

Acknowledgments

Financial supports from National Natural Science Foundation of China (No. 41807340), the National Key R&D Program of China (Nos. 2019YFC0408200, 2016YFC0402505), and National Water Pollution Control and Treatment Science and Technology Major Project (No. 2017ZX07207002) are acknowledged.

Appendix A. Supplementary data

Supplementary material related to this article can be found, in the online version, at doi:https://doi.org/10.1016/j.cclet.2021.01.012.

References

[1] C.M. Manaia, J. Rocha, N. Scaccia, et al., Environ. Int. 115 (2018) 312–324.
[2] S.M. Zainab, M. Junaid, N. Xu, et al., Water Res. 187 (2020) 116455.
[3] J. Xu, Y. Qi, C. Wang, et al., Appl. Catal. B 241 (2019) 178–186.
[4] F. Yu, L. Wang, Q. Xing, et al., Chin. Chem. Lett. 31 (2020) 1648–1653.
[5] Y. Li, S. Wang, W. Chang, et al., Appl. Catal. B 274 (2020) 119116.
[6] C. Yang, Z. Xue, J. Qin, et al., Appl. Catal. B 259 (2019) 118094.
[7] F. Chen, Z.Y. Ma, L.Q. Ye, et al., Adv. Mater. 32 (2020) 1908350.
[8] M. Chen, C. Guo, S. Hou, et al., Appl. Catal. B 266 (2020) 118614.
[9] V. Kuroki, G.E. Bosco, P.S. Fadini, et al., J. Hazard. Mater. 274 (2014) 124–131.
[10] L. Song, C. Guo, T. Li, et al., Ceram. Int. 43 (2017) 7901–7907.
[11] N. Tian, H. Huang, S. Wang, et al., Appl. Catal. B 267 (2020) 118697.
[12] S. Sun, J. Li, P. Song, et al., Appl. Surf. Sci. 500 (2020) 143985.
[13] Y. Cao, Q. Zheng, Z. Rao, et al., Chin. Chem. Lett. 31 (2020) 2689–2692.
[14] J. Chen, J. Zhan, Y. Zhang, et al., Chin. Chem. Lett. 30 (2019) 735–738.
[15] S. Luo, J. Ke, M. Yuan, et al., Appl. Catal. B 221 (2018) 215–222.
[16] H. Yi, M. Yan, D. Huang, et al., Appl. Catal. B 250 (2019) 52–62.
[17] W. Xue, D. Huang, J. Li, et al., Chem. Eng. J. 373 (2019) 1144–1157.
[18] B. He, H. Liu, Z. Lin, et al., Chem. Eng. J. 359 (2019) 924–932.
[19] Q. Liu, T. Chen, Y. Guo, et al., Appl. Catal. B 193 (2016) 248–258.
[20] S. Wang, X. Han, Y. Zhang, et al., Small Struct. 61 (2020) 200–249.
[21] Q. Zhou, Y. Song, N. Li, et al., Chem. Eng. J. 8 (2020) 7921–7927.
[22] S. Yan, Y. Shi, Y. Tao, et al., Chem. Eng. J. 359 (2019) 933–943.
[23] H. Dong, X. Zhang, J. Li, et al., Appl. Catal. B 263 (2020) 118270.
[24] L. Lai, H. Ji, H. Zhang, et al., Appl. Catal. B 282 (2021) 119559.
[25] M. Samy, M.G. Ibrahim, M. Gar Alalm, et al., Chem. Eng. J. 395 (2020) 124974.
[26] F. Damiri, S. Dobaradaran, S. Hashemi, et al., Ultrason. Sonochem. 68 (2020) 105187.
[27] S. Noor, M. Waseem, U. Rashid, et al., Chin. Chem. Lett. 25 (2014) 819–822.
[28] D. Kanakaraju, J. Kockler, C.A. Motti, et al., Appl. Catal. B 166-167 (2015) 45–55.